

Preparation, Structural Characterization, and Electrical Conductivity of Highly Ion-Conducting Glasses and Glass Ceramics in the System $\text{Li}_{1+x}\text{Al}_x\text{Sn}_y\text{Ge}_{2-(x+y)}(\text{PO}_4)_3$

Silvia H. Santagneli,* Helio V. A. Baldacim, and Sidney J. L. Ribeiro

LaMF, Instituto da Química, UNESP, Araraquara, SP, Brazil

Swarup Kundu and Ana Candida Martins Rodrigues

Departamento de Engenharia de Materiais, Universidade Federal de São Carlos, SP, Brazil

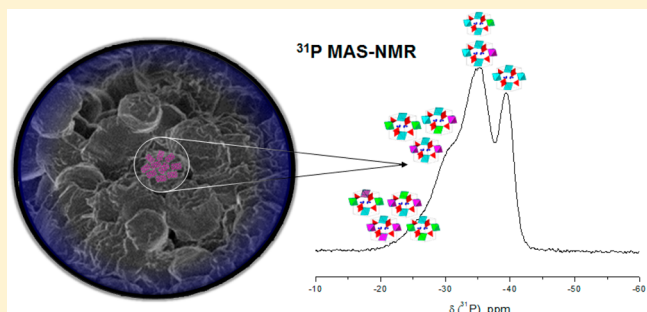
Carsten Doerenkamp and Hellmut Eckert

Instituto de Física de São Carlos, Universidade de São Paulo, São Carlos, SP, Brazil

Institut für Physikalische Chemie, WWU, Münster, Germany

S Supporting Information

ABSTRACT: Highly ion conducting glass-ceramics, crystallizing in the Na-superionic conducting (NASICON) structure, have been prepared in the system $\text{Li}_{1+x}\text{Al}_x\text{Sn}_y\text{Ge}_{2-(x+y)}(\text{PO}_4)_3$ by crystallization of glassy precursor samples. For modest substitution levels ($y = 0.25$), these crystalline solid solutions show slightly higher electrical conductivity than corresponding samples without Sn, supporting the rationale that the lattice expansion associated with the substitution of Ge by its larger homologue Sn can enhance ionic conductivity. Higher Sn substitution levels ($y = 0.45$) do not result in any improvement. The glass-to-crystal transition has been characterized in detail by multinuclear single and double resonance NMR experiments. While substantial changes in the ^{31}P and ^{27}Al MAS NMR spectra indicate that the crystallization of the glasses is accompanied by significant modifications in the local environments of the phosphate and the aluminum species, the dipolar solid state NMR experiments indicate that the structures of both phases are dominated by Ge–O–P, Sn–O–P, and Al–O–P connectivities. Substitution of Ge by Al and Sn in the crystalline NASICON structure results in a binomial distribution of multiple phosphate environments, which differ in the number of P–O–Ge, P–O–Al, and P–O–Sn linkages. While there is no chemical shift discrimination between P–O–Al and P–O–Sn linkages, an unambiguous distinction is possible on the basis of $^{31}\text{P}\{^{27}\text{Al}\}$ rotational echo adiabatic passage double resonance (REAPDOR) experiments.



INTRODUCTION

Lithium-ion battery technology is now being widely used in applications of great diversity, ranging from chemical sensing devices to large-scale energy storage equipment.^{1–6} Solid-state electrolytes, such as polymeric ion conductors and lithium-based glasses and glass-ceramics are being used in such devices due to rich opportunities for tailoring physicochemical properties through compositional adjustment. In particular, crystalline materials based on NASICON (Na super ionic conductor)-type crystalline frameworks provide high lithium ion mobilities,^{7–16} resulting in applications as separator materials in current Li/air battery prototypes.^{17–21} Their utility for solid electrolyte battery applications stems from the opportunity of preparing dense, nonporous glass-ceramics of glassy precursors by appropriate annealing protocols.^{7–10,12,13}

While ionic conductivities of the glassy precursor materials are lower by several orders of magnitude, the synergy of a highly conductive crystalline phase embedded in a mechanically stable, dense glass matrix, offers some technological benefits. The rhombohedral parent compound $\text{LiGe}_2(\text{PO}_4)_3$ possesses only moderate electrical conductivity; however, numerous chemical modifications have been introduced to modify and optimize the electrical conductivities of these materials. In particular, the aliovalent substitution of Ge^{4+} (or Ti^{4+}) by $\text{Al}^{3+} + \text{Li}^+$ introduces new lithium ions on the Li(2) sites (vacant in the structure of parent $\text{LiGe}_2(\text{PO}_4)_3$), producing a considerable

Received: May 12, 2016

Revised: June 16, 2016

Published: June 30, 2016



ACS Publications

© 2016 American Chemical Society

14556

DOI: 10.1021/acs.jpcc.6b04839
J. Phys. Chem. C 2016, 120, 14556–14567

enhancement in the electrical conductivity.^{7–16} Various other cation or anion substitution processes have been explored, extending the range of highly conductive members of this solid electrolyte family.^{22–38} Numerous of these studies have benefitted greatly from the potential of solid state NMR methods to provide information about structural details and to characterize ionic mobilities.^{31–38}

In the present contribution, we study the isovalent substitution of Ge⁴⁺ by its larger homologue Sn⁴⁺. The study is based on the rationale that the expected increase in lattice parameters may expand the size of the cation migration path bottleneck, resulting in increased cationic mobilities and hence higher electrical conductivities.^{25,39} Furthermore, replacement of expensive Ge by its cheaper homologue Sn is economically advisable. In this work we present our results on glasses and glass-ceramics of the system Li_{1+x}Al_xSn_yGe_{2-(x+y)}(PO₄)₃ (LASGP). The structural aspects of the glass-to-crystal transition and the related consequences of the Ge → Sn substitution have been examined by X-ray diffraction and multinuclear solid state NMR single and double-resonance experiments, on the basis of which the proposed cation substitution models are examined in a quantitative fashion. The ionic conductivities of the glass-ceramics have been measured by impedance spectroscopy and related to ionic mobility trends probed by temperature dependent static ⁷Li NMR.

■ EXPERIMENTAL SECTION

Glass and Glass-Ceramics Preparation. Glasses were prepared in 10 g batches from Li₂CO₃ (Riedel-de Haen, 99%), NH₄H₂PO₄ (Alfa Aesar, 98%), GeO₂ (Alfa Aesar, 99.999%), Al₂O₃ (Merck, 99.9%), and SnO₂ (Sigma-Aldrich 99.9%). The powdered starting materials were mixed and heated in a platinum crucible in three steps: (1) at 270 °C for 4 h to eliminate NH₃ and H₂O; (2) at 700 °C for 1 h to eliminate CO₂; and (3) at 1400–1600 °C for melting. The melt was kept at this temperature for 60 min to ensure homogenization and fining and was subsequently cooled rapidly in a brass mold. Macroscopically homogeneous glasses were obtained with a thickness of 3 mm. The amorphous state was confirmed by the absence of sharp X-ray diffraction peaks. The glass-ceramics were obtained from heat treatment of the glass. For the electrical conductivity measurements, polished pieces of the glass were inserted in a preheated furnace at the crystallization peak temperature (T_p) (known from the DSC curve of the glass) and kept at this temperature for 1 h. Other crystallized glass specimens were obtained by heating the glass samples with rate of 10 K min⁻¹ in a conventional furnace up to T_p and kept at this temperature for 2 h. No significant differences were observed in the NMR spectra between these two protocols.

Glass and Glass-Ceramics Characterization. Glass transition and crystallization temperatures were measured in a NETZSCH calorimeter model STA Jupiter 449 F3, using a heating rate of 10 K min⁻¹. X-ray diffraction (XRD) analysis was employed to identify the crystalline phases of the glass-ceramics using a SIEMENS Diffractometer (D 5000-DIFFRAC PLUS XRD). The measurements were carried out by using Ni-filtered Cu K α radiation generated at 30 mA and 40 kV, integration time at 2 s and 0.050° step. FT-Raman scattering measurements were obtained with a RAMII - BRUKER instrument, operating with a Nd/YAG-laser at 1064 nm. The micrograph images were obtained in a high-resolution scanning microscope model FEG-MEV; JEOL model 7500F.

Solid State NMR. High resolution solid state NMR spectra were measured at room temperature on a Bruker Avance III 400WB HD spectrometer, using a commercial 4 mm triple resonance MAS NMR probe. Typical spinning speeds were 12.0 to 14.0 kHz. Signal deconvolutions into Gaussian components were performed using the DMFIT software package.⁴⁰ ³¹P NMR measurements were carried out at 162.0 MHz, using $\pi/2$ pulses of 3.1 μ s length and a recycle delay of 200 s. Chemical shifts are reported relative to 85% H₃PO₄. ¹¹⁹Sn MAS NMR spectra were measured at 149.2 MHz using $\pi/2$ pulses of 2.2 μ s length and a recycle delay of 30 s. Chemical shifts are reported relative to crystalline SnO₂ (−604.3 ppm against tetramethyl tin). ²⁷Al MAS NMR measurements were carried out at 104.3 MHz. One-dimensional spectra were acquired using small flip-angle pulses of 1.2 μ s length and a recycle delay of 2 s. 2-D Triple Quantum Magic Angle Spinning (TQMAS) spectra were measured using the three-pulse z-filtering variant^{41,42} and rotor-synchronized acquisition of the indirect dimension with the following acquisition parameters: pulse lengths 4.4 to 5.2 μ s and 1.9 to 2.2 μ s for the first and second pulses applied with a ²⁷Al nutation frequency of 50 kHz and 10 μ s for the soft detection pulse applied with a ²⁷Al nutation frequency of 12 kHz. Sampling in the t₁ dimension was done with a dwell time of 21 ms. Data are presented in the sheared mode by projecting 2D contours for each individual site onto the F1 and F2 axes. To quantify the strength of ²⁷Al–³¹P magnetic dipole–dipole interactions, ²⁷Al{³¹P} rotational echo double resonance (REDOR)⁴³ and ³¹P{²⁷Al} rotational echo adiabatic passage double resonance (REAPDOR)⁴⁴ experiments were conducted using standard pulse sequences from the literature.⁴⁵ To optimize rf-homogeneity only the middle third of the 4 mm MAS rotor was filled with sample. Optimum π pulse lengths for the decoupling channel were set by maximizing the REDOR difference signal ΔS at a chosen dephasing time. The π -pulse lengths of ³¹P and ²⁷Al were 5.4–6.2 and 4.8–5.6 μ s, respectively. In the REDOR experiments, phase cycling according to the XY4 scheme was used for the ³¹P recoupling pulses. Normalized difference signal intensities $\Delta S/S_0$ (corresponding to the signal amplitudes without (S_0) and with (S) ³¹P pulsed irradiation) were plotted as a function of dipolar evolution time NT_r , and second moment values M_2 were extracted from the parabolic fits to the initial decay regime ($0 \leq \Delta S/S_0 \leq 0.3$), as previously described.⁴⁶ ³¹P{²⁷Al} REAPDOR NMR experiments were done at 12.0 kHz, employing $\pi/2$ pulses for ³¹P of 2.8–3.1 μ s length and ²⁷Al adiabatic pulses of 27.8 μ s length. The experiments were conducted at a ²⁷Al nutation frequency of 60 kHz measured on a liquid sample. For an analysis of the resulting REAPDOR curves, the simulation package SIMPSON⁴⁷ was used to estimate average numbers of P–O–Al linkages for each resolved ³¹P resonance. Variable temperature static ⁷Li NMR spectra were measured at 94.2 MHz, using an Agilent 240 MHz spectrometer.

Electrical Conductivity Measurements. For electrical conductivity measurements, all the specimens were subjected to the following sample preparation procedure: they were cut into rectangular shapes, and the glassy samples were subjected to heat-treatment for 1 h at their respective peak crystallization temperature, in a preheated furnace to avoid uncontrolled nucleation during ramping. The obtained glass-ceramics were polished and coated with sputtered gold electrodes on the two opposite parallel surfaces. Temperature dependent electrical conductivity measurements were carried out on samples with

thicknesses varying from 1.5 to 2.6 mm, using an impedance analyzer (Novocontrol Technologies Alpha-A, Hundsangen, Germany), operating in the frequency range of 2 Hz–40 MHz and in the temperature range of 30–200 °C. The instrument was attached with an active sample cell holder (ZGS-BDCS-140801, Novocontrol Technologies) and computer interfaced with “WinFit” software for data acquisition. The sample was sandwiched between two circular gold plated electrodes.

RESULTS AND DISCUSSION

Macroscopic Properties. The glasses obtained after melting were visually transparent, homogeneous, and chemically stable. Table 1 summarizes the glass compositions, their

Table 1. Sample Compositions, Glass Transition Temperatures, T_g , Crystallization Onset Temperature, T_x , and Peak Temperature, T_p (± 5 K), Obtained on Glassy Samples with Compositions $\text{Li}_{1+x}\text{Al}_x\text{Sn}_y\text{Ge}_{2-(x+y)}(\text{PO}_4)_3$

composition	T_g (°C)	T_x (°C)	T_p (°C)
$x = 0 y = 0$	520	662	665
$x = 0 y = 0.5$	544	604	616
$x = 0.05 y = 0.45$	511	605	618
$x = 0.25 y = 0.45$	500	609	623
$x = 0.25 y = 0.25$	518	622	628/651
$x = 0.25 y = 0$	547	635	642

glass transition temperatures, T_g , and the crystallization onset and peak temperatures, T_x and T_p . The DSC results are summarized in Figure 1. For the tin-free samples, the results are in good agreement with the literature.³³ Partial replacement of Ge by either Sn or Al results in increased T_g values. In the context of the solid-state NMR results to be discussed below, this increase may be related to an increased average coordination number owing to a higher fraction of six-

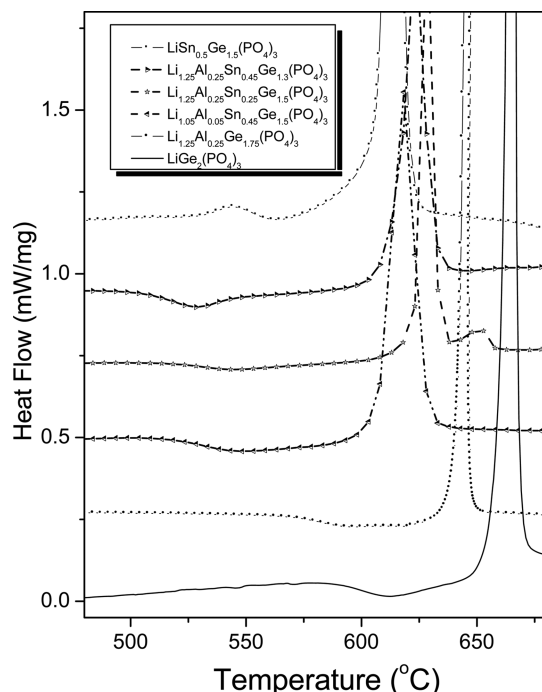


Figure 1. DSC curves of glassy samples with compositions $\text{Li}_{1+x}\text{Al}_x\text{Sn}_y\text{Ge}_{2-(x+y)}(\text{PO}_4)_3$.

coordinated network former species (Ge, Sn, and Al) as compared to pure LGP glass. In contrast, the trend toward lower T_g values in those samples in which Sn and Al are simultaneously present is more difficult to rationalize at the present time. Glassy $\text{LiGe}_2(\text{PO}_4)_3$ crystallizes at $T_p = 665$ °C for a 10 K min⁻¹ heating rate. Substitution of Ge^{4+} by Sn^{4+} tends to decrease both T_g and T_p , for Al-containing compositions.

To obtain the glass-ceramics, the bulk vitreous samples were annealed at T_p for 2 h, resulting in opaque samples that were fully crystallized. Figure 2 shows the microstructures of these glass-ceramics. Average particle sizes were 200 nm in the case of $\text{LiGe}_2(\text{PO}_4)_3$ and 800 nm–1400 nm for all the other fully crystallized glass-ceramics. Results from SEM indicate that the samples show very dense microstructures with very few pores and cracks.

X-ray powder diffraction patterns (Figure 3) confirm the dominant formation of single-phase materials with the NASICON structure (JCPDS no. 80-1922) in most cases.^{33,44} Also small fractions of crystalline AlPO_4 , SnP_2O_7 , and GeO_2 (JCPDS file cards: 01-073-6179, 00-029-1352, and 04-0497)^{48,49} can be identified in some of the samples, whereas the crystalline phase $\text{LiSn}_2(\text{PO}_4)_3$ (JCPDS file 87-2078) is not observed. Most importantly, however, the XRD data clearly confirm the successful substitution of germanium by tin within the NASICON structure, resulting in increased average lattice plane distances, typical of solid solutions. Table 2 summarizes the lattice constants, refined in the space group $R\bar{3}c$ by comparing the experimental data with simulated powder patterns. As expected, the partial substitution of Ge by Sn results in larger unit cell volumes. According to Winand et al.⁵⁰ a limiting difference of $\Delta r = 0.1$ Å between the ionic radii is considered a good criterion for forming a solid solution. Considering the ionic radii of 0.53, 0.535, and 0.69 Å for Ge^{4+} , Al^{3+} , and Sn^{4+} , respectively, this limit has been considerably exceeded in the present solid solutions.

Glass Structure Elucidation by Solid State NMR. The ³¹P MAS NMR spectra of the glassy $\text{Li}_{1+x}\text{Sn}_y\text{Al}_x\text{Ge}_{2-(x+y)}(\text{PO}_4)_3$ samples are shown in Figure 4. Broad Gaussian-shaped curves are obtained, whose chemical shift is centered near -23 to -29 ppm, depending on the composition (see Table 3). Substitution of germanium by tin has the effect of shifting the center of gravity of the signals toward less negative values. The spectra of the tin-free samples appear slightly asymmetric, suggesting some discrimination of different sites; however, the resolution is insufficient to try any deconvolution analysis. The line widths reflect isotropic chemical shift distributions arising from variations in the local environments of the phosphate species, which can connect to Ge, Sn, Al, and P. The ³¹P chemical shifts observed in the glassy state differ significantly from those observed in the isochemical crystalline compounds (see below). This result indicates that there are significant differences in the local phosphate environments between both phases. More insights into this difference can be obtained from Raman spectra, included in the Supporting Information (see Figure S1): in the glassy phase, these spectra show a band near 1280 cm⁻¹ which can be attributed to the P=O stretching vibration of a P⁽³⁾-type (branching phosphate) unit.⁵¹ In contrast the crystallized samples, in which all the phosphate species belong to the P⁽⁴⁾-type do not show any band in this region.⁵² Indeed, the ³¹P chemical shifts observed in our glasses are consistent with those previously found for P⁽³⁾ units in other alkali germanophosphate glasses.⁵¹ Thus, we conclude

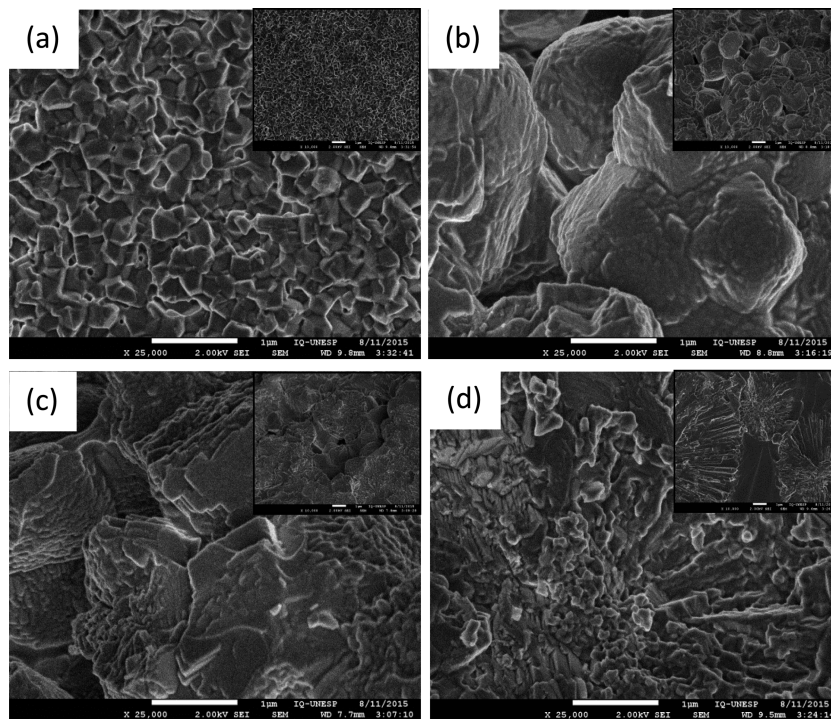


Figure 2. Microstructure of glass-ceramics obtained by thermal treatment at T_c for 2 h having the compositions (a) $\text{LiGe}_2(\text{PO}_4)_3$, (b) $\text{Li}_{1.25}\text{Al}_{0.25}\text{Sn}_{0.25}\text{Ge}_{1.5}(\text{PO}_4)_3$, (c) $\text{Li}_{1.25}\text{Al}_{0.25}\text{Sn}_{0.45}\text{Ge}_{1.5}(\text{PO}_4)_3$, and (d) $\text{Li}_{1.05}\text{Al}_{0.25}\text{Sn}_{0.45}\text{Ge}_{1.5}(\text{PO}_4)_3$.

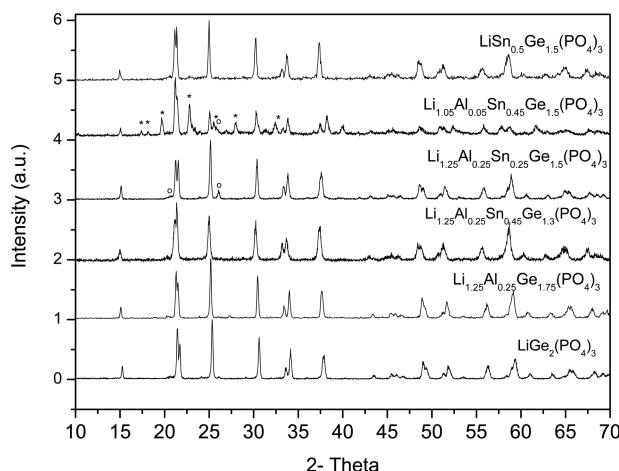


Figure 3. X-ray diffraction (XRD) patterns (scattering intensity versus diffraction angle 2 theta (degrees) of the of $\text{Li}_{1+x}\text{Al}_x\text{Sn}_y\text{Ge}_{2-(x+y)}(\text{PO}_4)_3$ glass-ceramics. The (*) indicate SnP_2O_7 and (°) GeO_2 crystalline phases.

that the glass to crystal transition in these NASICON type glass ceramics involves a transformation from $\text{P}^{(3)}_{3(\text{Ge},\text{Al},\text{Sn},\text{P})}$ to $\text{P}^{(4)}_{4(\text{Ge},\text{Al},\text{Sn})}$ units. In the glassy state the phosphate units are linked to Ge and Al atoms in mixed four, five, and six coordination as well as to six-coordinated Sn atoms, whereas in the crystalline state the P atoms are exclusively linked to six-coordinated atoms. The ^{19}Sn MAS NMR spectra are shown in Figure 5. Average chemical shift values, extracted from the centers of gravity are summarized in Table 3. The spectra for all the glass samples show broad symmetric resonances centered near -832 ppm, indicating that the Sn^{4+} ions are six-coordinated.^{53,54} There is no evidence of Sn^{2+} species.

The ^{27}Al MAS NMR spectra (Figure 6) indicate that the aluminum atoms are found in four-, five-, and six-coordination,

Table 2. Determined Unit Cell Lengths (in Å) and Angles (in Degrees) Obtained by Comparing the X-ray Powder Diffraction Data to Simulated Patterns in the Space Group R-3c (Hexagonal Setting) of the Crystalline $\text{Li}_{1+x}\text{Al}_x\text{Sn}_y\text{Ge}_{2-(x+y)}(\text{PO}_4)_3$ Samples

compositions $x = \text{Al};$ $y = \text{Sn}$	unit cell lengths (Å)			angles (degrees)		
	a	b	c	α	β	γ
$x = 0 y = 0$	8.2501	8.2501	20.5870	90	90	120
$x = 0 y = 0.5$	8.3238	8.3238	20.7025	90	90	120
$x = 0.05 y = 0.45$	8.3074	8.3074	20.6716	90	90	120
$x = 0.25 y = 0.45$	8.3203	8.3203	20.7515	90	90	120
$x = 0.25 y = 0.25$	8.2958	8.2958	20.7431	90	90	120
$x = 0.25 y = 0$	8.2553	8.2553	20.5226	90	90	120

as previously found in LAGP glasses.^{33,34} Table S1 (Supporting Information) summarizes the relevant line shape parameters. The TQMAS spectrum of $\text{Li}_{1.25}\text{Al}_{0.25}\text{Sn}_{0.25}\text{Ge}_{1.5}(\text{PO}_4)_3$ glass is shown in Figure S2 (Supporting Information). Figure 6 indicates that substitution of Ge by Sn tends to increase the fractions of four-coordinated Al in the glass phase.

Figure S3 shows $^{27}\text{Al}\{^{31}\text{P}\}$ REDOR data. The individual curves obtained for the different Al coordination numbers are indistinguishable within experimental error, suggesting that the strengths of the $^{27}\text{Al}-^{31}\text{P}$ magnetic dipole–dipole couplings are very similar to each other, just as observed by Schröder et al.³³ The M_2 ($^{27}\text{Al}\{^{31}\text{P}\}$) values near $5 \times 10^6 \text{ rad}^2 \text{ s}^{-2}$ are comparable to those measured in other LAGP glasses^{33,34} thus suggesting that the network structure is dominated by Al–O–P connectivity and few Al–O–Ge (or Al–O–Sn) linkages occur. For these reasons, we refrained from attempting $^{19}\text{Sn}\{^{27}\text{Al}\}$ double resonances studies, which would in any event give rather weak dipolar coupling effects owing to the low levels of both aluminum and tin in our samples.

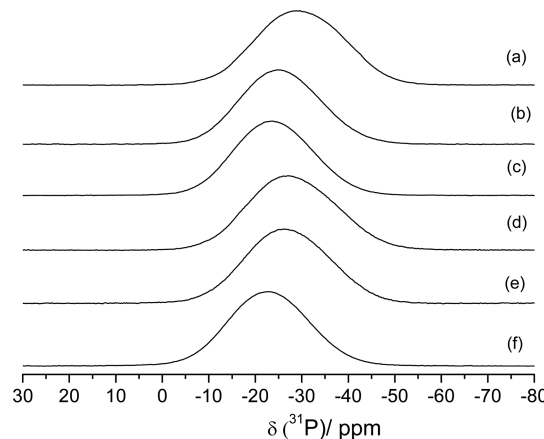


Figure 4. ^{31}P MAS NMR spectra of glasses with the compositions: (a) $\text{LiGe}_2(\text{PO}_4)_3$, (b) $\text{LiSn}_{0.5}\text{Ge}_{1.5}(\text{PO}_4)_3$, (c) $\text{Li}_{1.05}\text{Al}_{0.05}\text{Sn}_{0.45}\text{Ge}_{1.5}(\text{PO}_4)_3$, (d) $\text{Li}_{1.25}\text{Al}_{0.25}\text{Ge}_{1.75}(\text{PO}_4)_3$, (e) $\text{Li}_{1.25}\text{Al}_{0.25}\text{Sn}_{0.25}\text{Ge}_{1.5}(\text{PO}_4)_3$, and (f) $\text{Li}_{1.25}\text{Al}_{0.25}\text{Sn}_{0.45}\text{Ge}_{1.3}(\text{PO}_4)_3$.

Table 3. ^{31}P NMR Chemical Shifts δ_{iso} (Centers of Gravity) of the Glassy and ^{119}Sn NMR Chemical Shifts of the Glassy and the Crystalline Samples with Compositions $\text{Li}_{1+x}\text{Al}_x\text{Sn}_y\text{Ge}_{2-(x+y)}(\text{PO}_4)_3$

composition $y = \text{Sn}$; $x = \text{Al}$	$\delta_{\text{iso}}^{31}\text{P}/\text{ppm}$		$\delta_{\text{iso}}^{119}\text{Sn}/\text{ppm}$	
	glass (± 1 ppm)	glass (± 5 ppm)	glass (± 1 ppm)	crystal (± 1 ppm)
$x = 0 y = 0$	-29.6			
$x = 0 y = 0.5$	-24.7	-838	-784	
$x = 0.05 y = 0.45$	-23.7	-836	-789	
$x = 0.25 y = 0.45$	-22.7	-836	-789	
$x = 0.25 y = 0.25$	-25.1	-831	-789	
$x = 0.25 y = 0$	-27.0			

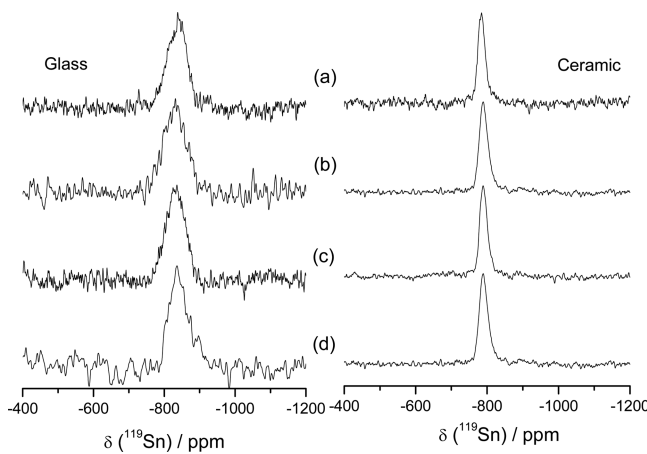


Figure 5. ^{119}Sn MAS NMR spectra of glassy and crystalline samples having the compositions: (a) $\text{LiSn}_{0.5}\text{Ge}_{1.5}(\text{PO}_4)_3$, (b) $\text{Li}_{1.25}\text{Al}_{0.25}\text{Sn}_{0.25}\text{Ge}_{1.5}(\text{PO}_4)_3$, (c) $\text{Li}_{1.05}\text{Al}_{0.05}\text{Sn}_{0.45}\text{Ge}_{1.5}(\text{PO}_4)_3$, and (d) $\text{Li}_{1.25}\text{Al}_{0.25}\text{Sn}_{0.45}\text{Ge}_{1.3}(\text{PO}_4)_3$.

NMR Studies of the Crystalline Materials. The ^{119}Sn MAS NMR spectra of the crystalline samples (Figure 5) reveal single sharp resonances at -788 ppm, consistent with Sn^{4+} ions in a six-coordinated (SnO_6) type environment.^{53,54} The chemical shifts do not vary with tin content in the crystalline materials, indicating uniform substitution of Sn within the Ge sites of the NASICON lattice. Again, we observe, however, a

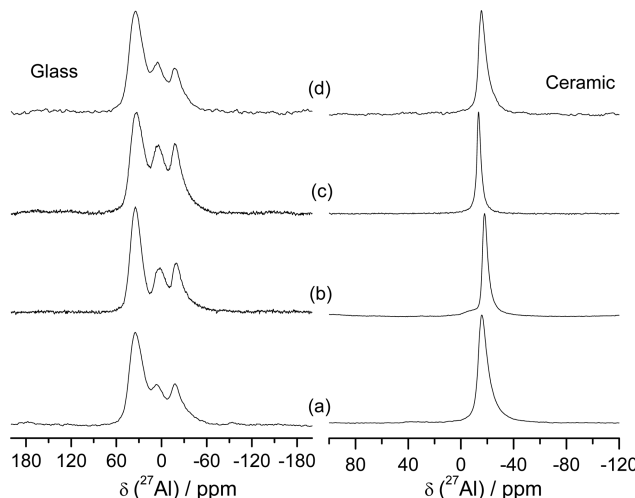


Figure 6. ^{27}Al MAS NMR spectra of glassy and crystalline samples with the compositions (a) $\text{Li}_{1.25}\text{Al}_{0.25}\text{Sn}_{0.45}\text{Ge}_{1.3}(\text{PO}_4)_3$, (b) $\text{Li}_{1.25}\text{Al}_{0.25}\text{Sn}_{0.25}\text{Ge}_{1.5}(\text{PO}_4)_3$, (c) $\text{Li}_{1.25}\text{Al}_{0.25}\text{Ge}_{1.75}(\text{PO}_4)_3$, and (d) $\text{Li}_{1.05}\text{Al}_{0.05}\text{Sn}_{0.45}\text{Ge}_{1.5}(\text{PO}_4)_3$.

substantial difference between the chemical shifts in the crystalline and the isochemical glassy phases. The ^{27}Al MAS NMR spectra (Figure 6) indicate a single peak at isotropic chemical shifts near -14 ppm, corresponding to the regular AlO_6 octahedral sites in the NASICON structure. Figure S2 (Supporting Information) shows typical ^{27}Al TQMAS-NMR spectra, and Table S2 (Supporting Information) summarizes the isotropic chemical shifts and second order quadrupolar effect (SOQE) values extracted from these data.

The $^{27}\text{Al}\{^{31}\text{P}\}$ REDOR curves of all the glassy and crystalline phases are shown in Figures S3 and S4 (Supporting Information). The second moments derived from them ($5.0 \pm 0.5 \times 10^6 \text{ rad}^2 \text{ s}^{-2}$) indicate the dominance of Al–O–P coordination, consistent with previous measurements on crystallized LAGP phases.³³ The theoretically expected value for LGP is $M_2 = 7.4 \times 10^6 \text{ rad}^2 \text{ s}^{-2}$, if the P–O–Al distances are identical to the P–O–Ge distance of 318 pm in LGP. However, as previously discussed,³³ the difference observed between the experimental and theoretical M_2 values might be attributable to some local distortions, resulting in Al–O–P distances that are somewhat longer than the above value.

The ^{31}P MAS NMR spectra of the crystallized $\text{Li}_{1+x}\text{Al}_x\text{Sn}_y\text{Ge}_{2-(x+y)}(\text{PO}_4)_3$ samples are summarized in Figure 7. Multiple peaks are observed for all samples with $x > 0$, and the deconvolution components are summarized in Table 4. For crystalline $\text{LiGe}_2(\text{PO}_4)_3$, we observe a single resonance line at -42.1 ppm, representing P sites coordinated to four $\text{Ge}^{(6)}$ next nearest neighbors, $\text{P}^{(4)}_{4\text{Ge}}$. As discussed in ref 33, substitution of Ge by Al generates additional local environments, $\text{P}^{(4)}_{(4-n)\text{Ge},n\text{Al}}$ ($1 \leq n \leq 4$) which give rise to separate line shape contributions observed in the region between -20 and -43 ppm. For those tin-free glass-ceramics the assignments of the distinct resonances were made based on $^{31}\text{P}\{^{27}\text{Al}\}$ REAPDOR experiments, and the relative intensity profiles could be well-described by a binomial distribution.³³

As for the present tin-containing samples Figure 7 indicates that substitution of Ge by Sn has a numerically similar effect on the NMR spectra as the substitution of Ge by Al. Thus, the peak multiplicity observed in these spectra arises from the formation of $\text{P}^{(4)}_{(4-n-m)\text{Ge},n\text{Al},m\text{Sn}}$ sites. As the substitution of Ge by either Al or Sn has essentially the same effects on the ^{31}P

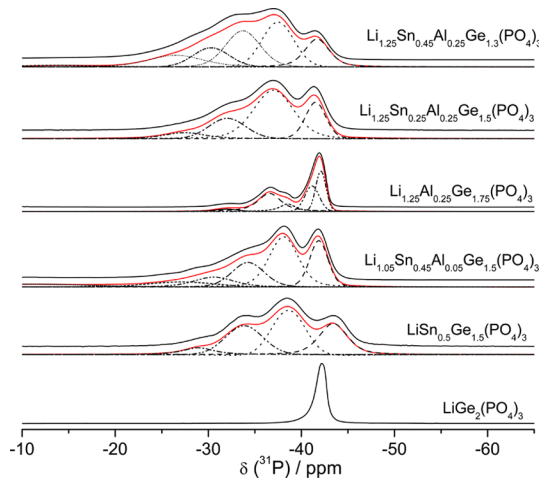


Figure 7. ^{31}P MAS NMR spectra of fully crystallized glass-ceramics having the composition $\text{Li}_{1+x}\text{Al}_x\text{Sn}_y\text{Ge}_{2-(x+y)}(\text{PO}_4)_3$. Dashed curves indicate deconvolution components.

Table 4. Deconvolution Results (Chemical Shifts, $\delta_{\text{iso}} \pm 0.5$ ppm, and Fractional Areas, $\pm 2\%$) of the ^{31}P MAS NMR Spectra Obtained on Crystalline $\text{Li}_{1+x}\text{Al}_x\text{Sn}_y\text{Ge}_{2-(x+y)}(\text{PO}_4)_3$ Samples

compositions $y = \text{Sn}$; $x = \text{Al}$	% area	$\delta_{\text{iso}} \text{ } ^{31}\text{P}/\text{ppm}$
$x = 0 \ y = 0$	100	-42.1
$x = 0 \ y = 0.5$	27.8	-43.4
	36.0	-38.6
	29.0	-33.9
	7.3	-28.9
$x = 0.05 \ y = 0.45$	20.2	-41.9
	36.1	-38.1
	18.5	-34.3
	10.0	-30.6
	7.2	-27.1
	7.5	-11.0
$x = 0.25 \ y = 0.45$	16.1	-41.7
	27.8	-37.5
	25.7	-33.7
	13.4	-30.3
	14.3	-26.5
	2.6	-13.6
$x = 0.25 \ y = 0.25$	20.0	-41.5
	53.5	-36.9
	18.9	-32.0
	7.6	-27.5
$x = 0.25 \ y = 0$	27.2	-42.1
	24.2	-41.1
	10.8	-38.5
	34.5	-36.6
	3.3	-31.9

chemical shifts, it is impossible to differentiate between phosphate sites with the same number of Ge neighbors but different numbers of Sn and Al neighbors. Thus, separate line shape components can only be resolved for $\text{P}^{(4)}_{(4-n-m)\text{Ge},(n+m)\text{Al/Sn}}$ sites. Neglecting the formation of minor amounts of AlPO_4 and GeO_2 in the present materials, we can compare the line shape intensity profiles (based on the integrated signal areas) with the corresponding populations predicted for binomial distributions, which are 32%: 42%: 21%: 4.5%: 0.5% for $n+m = 0, 1, 2, 3$, and 4, respectively, in all the samples with $x+y = 0.5$ and 18%, 38%,

31%, 11%, and 2% for $n+m = 0, 1, 2, 3$, and 4, respectively in the sample with $x+y = 0.7$. If we compare these numbers with the site populations given in Table 2, a generally satisfactory agreement can be noted. In addition, for each individual site characterized by the sum $n+m$, we must consider separate combinations of n and m with statistically predicted populations as follows:

$$[\text{P}^4_1] = [\text{P}^4_{1\text{Al}}] + [\text{P}^4_{1\text{Sn}}] = \left(\frac{x}{(x+y)} \right) + \left(\frac{y}{(x+y)} \right) \quad (1)$$

$$\begin{aligned} [\text{P}^4_2] &= [\text{P}^4_{(1\text{Al},1\text{Sn})}] + [\text{P}^4_{(2\text{Al})}] + [\text{P}^4_{(2\text{Sn})}] \\ &= \left[\left(\frac{x}{(x+y)} \times \frac{y}{(x+y)} \right) \times 2 + \left(\frac{x}{(x+y)} \right)^2 \right. \\ &\quad \left. + \left(\frac{y}{(x+y)} \right)^2 \right] \end{aligned} \quad (2)$$

$$\begin{aligned} [\text{P}^4_3] &= [\text{P}^4_{(2\text{Al},1\text{Sn})}] + [\text{P}^4_{(3\text{Al})}] + [\text{P}^4_{(3\text{Sn})}] + [\text{P}^4_{(1\text{Al},2\text{Sn})}] \\ &= \left\{ \left[\left(\frac{y}{(x+y)} \right) \times \left(\frac{x}{(x+y)} \right)^2 \times 3 \right] \right. \\ &\quad \left. + \left(\frac{x}{(x+y)} \right)^3 + \left(\frac{y}{(x+y)} \right)^3 \right. \\ &\quad \left. + \left[\left(\frac{x}{(x+y)} \right) \times \left(\frac{y}{(x+y)} \right)^2 \times 3 \right] \right\} \end{aligned} \quad (3)$$

Table 5 summarizes the fractional peak areas predicted from the above equations for each of the various $\text{P}^4_{n\text{Al},m\text{Sn}}$ units for the samples under study. From these numbers we can compute the average number of P–O–Al linkages per phosphorus atom $\langle n_{\text{Al}}(\text{P}) \rangle$ (bin) = $\sum n f(\text{P}^4_{n\text{Al},m\text{Sn}})$ for each individual site as predicted by this binomial distribution.

The site assignments proposed in the present study agree with those previously made for tin-free samples³³ and are further confirmed by the $^{31}\text{P}\{^{27}\text{Al}\}$ REAPDOR experiments summarized in Figure 8. The resonances near -41 to -43 ppm show the weakest REAPDOR effect and are thus easily identified as $\text{P}^4_{4\text{Ge}}$ sites ($m+n=0$). In a similar vein, the moderate REAPDOR effect observed for the signal component near -37 to -38 ppm suggests its assignment to the site with $(m+n)=1$, and the yet larger REAPDOR effect observed for the peak near -34 ppm is consistent with $(n+m)=2$. For the sites with larger $n+m$ values the REAPDOR analysis becomes increasingly difficult because of increased signal overlap and generally low signal intensities. Nevertheless, as explained below, the REAPDOR experiments can provide useful experimental estimates of $\langle n_{\text{Al}}(\text{P}) \rangle$ for each $\text{P}^{(4)}_{(n+m)\text{Al/Sn}}$ site. This can be done by comparing the experimental REAPDOR data with a SIMPSON two-spin simulation based on an internuclear ^{31}P – ^{27}Al distance of 330 pm (instead of 318 pm we choose here the value chosen consistent with the $^{27}\text{Al}\{^{31}\text{P}\}$ REDOR data), the ^{27}Al nuclear electric quadrupolar coupling constant of 2.1 MHz estimated from the TQMAS data and the ^{27}Al nutation frequency used in the REAPDOR experiment (see solid curves in Figure 8). These simulations reveal that at all three compositions studied, for all the $\text{P}^{(4)}_{n+m}$ sites the

Table 5. Individual Fractional Contributions $f(P_{nAl,mSn}^4)$ for Each of the Various $P_{nAl,mSn}^4$ Sites to the Total Area of the NMR Signal of Each Resolved NMR Signal Component as Predicted by Binomial Statistics in Crystalline Samples with Compositions $Li_{1+x}Al_xSn_yGe_{2-(x+y)}(PO_4)_3$

compositions $y = Sn; x = Al$	P_{1Al}^4		$P_{1Al,1Sn}^4$			P_{2Al}^4			P_{2Sn}^4			$P_{1Al,2Sn}^4$			$P_{2Al,1Sn}^4$			P_{3Al}^4		
	P_{1Al}^4	P_{1Sn}^4	$P_{1Al,1Sn}^4$	P_{2Al}^4	P_{2Sn}^4	$P_{1Al,2Sn}^4$	$P_{2Al,1Sn}^4$	P_{3Al}^4	P_{3Sn}^4											
$x = 0 y = 0.5$	0	1.00	0	0	100	0	0	0	1.00	0	0	0	0	0	0	0	0	0	1.00	0
$x = 0.05 y = 0.45$	0.10	0.90	0.18	0.01	0.81	0.24	0.03	0	0	0.24	0.03	0	0	0.73	0	0	0	0	0	0.73
$x = 0.25 y = 0.45$	0.36	0.64	0.46	0.13	0.41	0.44	0.25	0.04	0.41	0.44	0.25	0.04	0.27	0	0	0	0	0	0	0.27
$x = 0.25 y = 0.25$	0.50	0.50	0.50	0.25	0.25	0.38	0.38	0.13	0.25	0.38	0.38	0.13	0.13	0.13	0	0	0	0	0	0.13
$x = 0.25 y = 0$	1.00	0	0	1.00	0	0	0	0	0	0	0	0	0	0	0	0	0	0	0	0

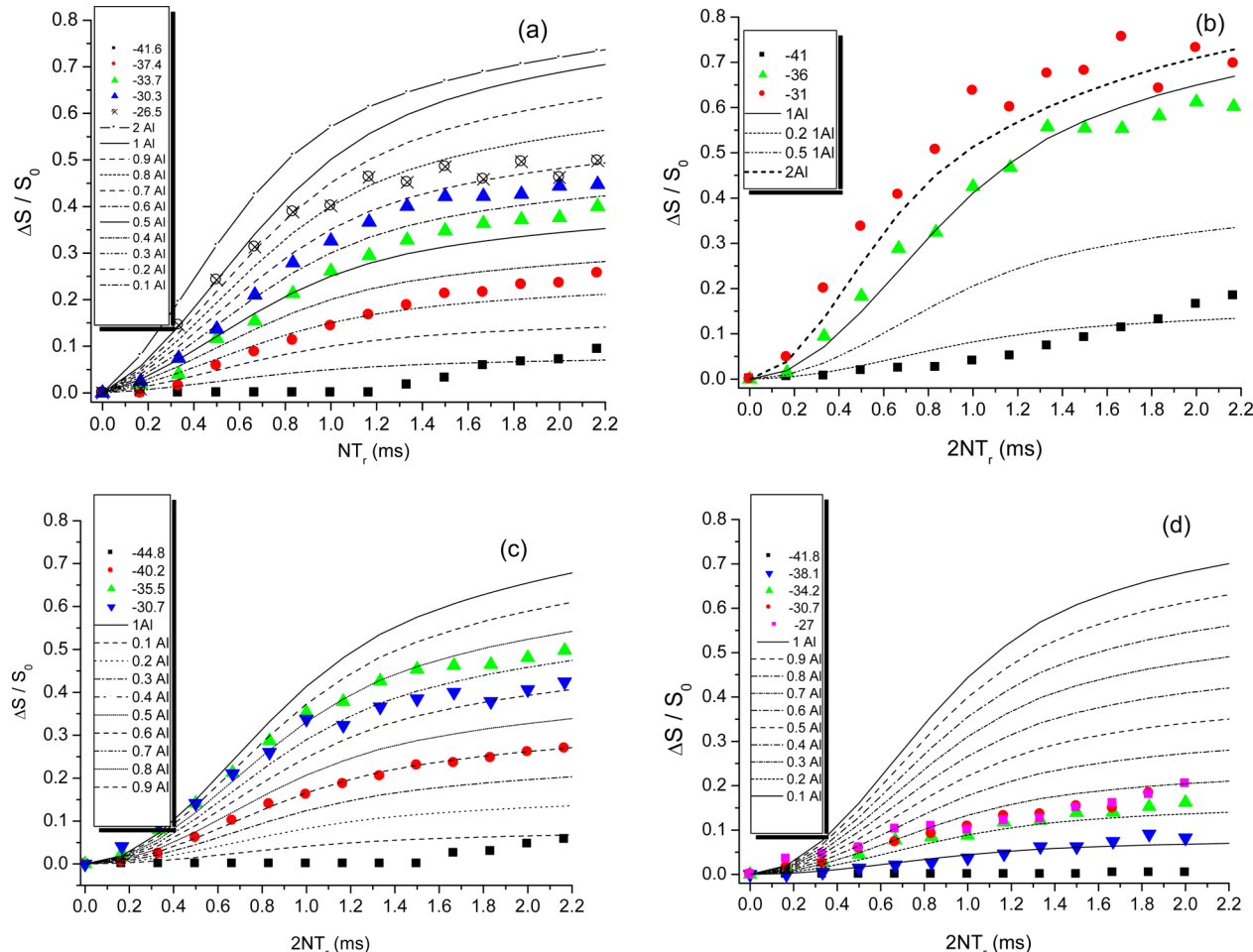


Figure 8. $^{31}P\{^{27}Al\}$ REAPDOR curves of fully crystallized samples with the following compositions: (a) $Li_{1.25}Al_{0.25}Sn_{0.45}Ge_{1.3}(PO_4)_3$, (b) $Li_{1.25}Al_{0.25}Ge_{1.75}(PO_4)_3$, (c) $Li_{1.25}Al_{0.25}Sn_{0.25}Ge_{1.5}(PO_4)_3$, and (d) $Li_{1.05}Al_{0.25}Sn_{0.45}Ge_{1.5}(PO_4)_3$. Curves denote simulated behavior for different fractions of P–O–Al linkages. See text for further details.

Table 6. Statistically Predicted and Experimentally Observed Values of $\langle n_{Al}(P) \rangle$ in Crystalline Samples with Compositions $Li_{1+x}Al_xSn_yGe_{2-(x+y)}(PO_4)_3$

compositions $y = Sn; x = Al$	P_0^4	$\langle n_{Al}(P_1^4) \rangle$		$\langle n_{Al}(P_2^4) \rangle$		$\langle n_{Al}(P_3^4) \rangle$	
		exp	stat	exp	stat	exp	stat
$x = 0 y = 0.5$	0	0	0	0	0	0	0
$x = 0.05 y = 0.45$	0	0.1 ± 0.05	0.10	0.2 ± 0.05	0.20	0.2 ± 0.1	0.30
$x = 0.25 y = 0.45$	0	0.3 ± 0.1	0.36	0.5 ± 0.2	0.72	0.7 ± 0.3	1.08
$x = 0.25 y = 0.25$	0	0.4 ± 0.1	0.50	0.9 ± 0.2	1.00	0.9 ± 0.3	1.50
$x = 0.25 y = 0$	0		1.00		2.00		3.00

strength of the average ^{31}P – ^{27}Al dipolar coupling is weaker than that expected for a single P–O–Al linkage. Thus, by comparing the experimental data for each site with correspond-

ing superpositions of REAPDOR curves for one and zero P–O–Al linkages, we can arrive at suitable experimental estimates of average $\langle n_{Al}(P) \rangle$ (exp) for each resolved site. These values

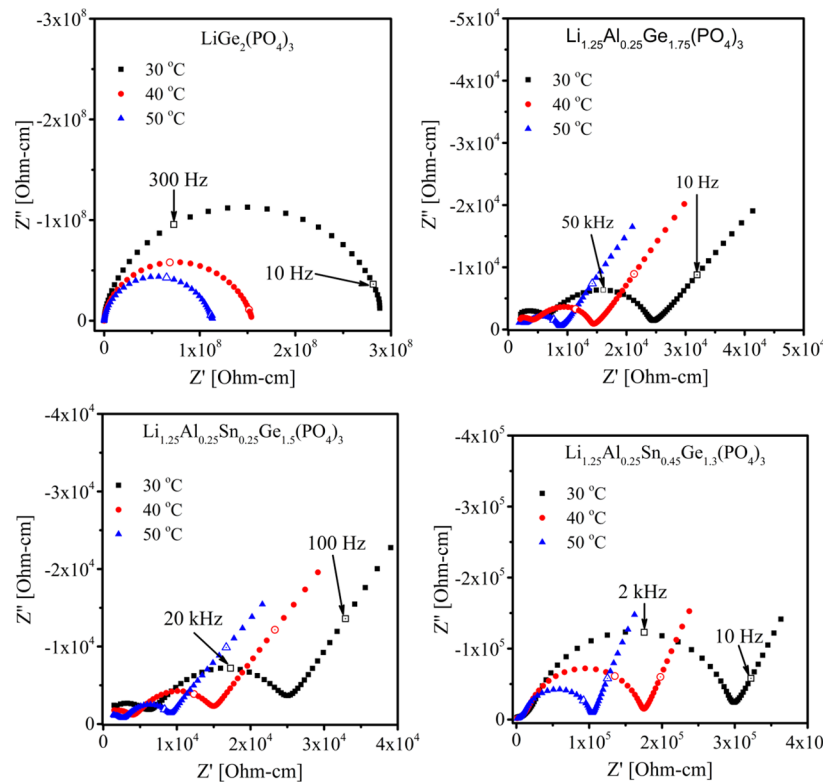


Figure 9. Examples of impedance complex plane plots (Nyquist diagrams) obtained at different temperatures for some of the investigated crystalline compositions of the $\text{Li}_{1+x}\text{Al}_x\text{Sn}_y\text{Ge}_{2-(x+y)}(\text{PO}_4)_3$ system. Open symbols correspond to indicated frequencies.

are summarized and compared with the statistically predicted values in Table 6.

While the agreement between $\langle n_{\text{Al}}(\text{P}) \rangle$ (exp) and $\langle n_{\text{Al}}(\text{P}) \rangle$ (bin) is reasonable overall, the experimental values tend to be somewhat smaller than the predicted values, particularly for P^4_{n+m} sites with $n+m > 1$. In part this discrepancy may arise from the larger errors associated with the deconvolution of these heavily overlapping resonances. Another explanation is suggested in connection with similar REAPDOR results obtained by Liu et al.³⁴ and Schröder et al.³³ on tin-free samples having the composition $\text{Li}_{1+x}\text{Al}_x\text{Ge}_{2-x}(\text{PO}_4)_3$. Those data also show that the effective local field generated by each ^{27}Al nucleus at a given ^{31}P site actually decreases significantly in the sequence $\text{P}^4_{1\text{Al}} > \text{P}^4_{2\text{Al}} > \text{P}^4_{3\text{Al}} > \text{P}^4_{4\text{Al}}$ indicating a systematic increase in the length of the P–O–Al linkages with increasing substitution level. Taking this fact into consideration the random distribution model can be judged to fit the experimental data quite satisfactorily. Thus, all the results obtained within the present study are consistent with the combined random substitution model $\text{Ge}^{4+} \rightarrow \text{Al}^{3+} + \text{Li}^+$ and $\text{Ge}^{4+} \rightarrow \text{Sn}^{4+}$. Within the stated limitations the present study demonstrates the utility of $^{31}\text{P}\{^{27}\text{Al}\}$ REAPDOR experiments to selectively quantify the average number of P–O–Al linkages that can be attributed to an individual ^{31}P resonance comprised of several overlapping individual components.

Electrical Conductivity. Figure 9 shows some examples of the complex impedance plots of the crystalline samples measured at different temperatures; complete documentation is found in the Supporting Information (Figures S6 and S7). Crystalline $\text{LiGe}_2(\text{PO}_4)_3$ exhibits only one single semicircle whereas all the other samples show two semicircles. The observed semicircle in the high frequency range corresponds to the bulk property of the sample and the semicircle in the low

frequency range is related to grain boundary effects. The complex data was fitted with the Z-view software to determine the electrical resistance (R), from which the bulk electrical conductivity (σ) was calculated via $\sigma = l/(R \cdot A)$, where l and A are the thickness and area of the sample, respectively. Activation energies E_σ were extracted from the slopes of linear Arrhenius plots ($\log \sigma$ vs $10^3/T$), see Figure 10. Figures 11 and Table 7 summarize the electrical conductivity at ambient temperature, as well as the activation energies and the pre-exponential factors of the Arrhenius expression. The comparison of the data for the $x = 0.25$, $y = 0$ and the $x = 0.25$, $y = 0.25$ samples indicates that low substitution levels of tin for

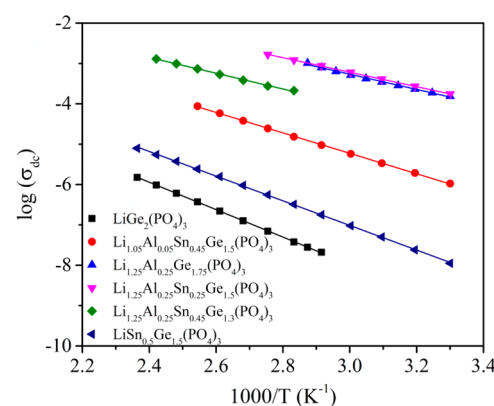


Figure 10. Arrhenius plots of grain conductivities obtained from the complex impedance plots of crystalline samples with compositions $\text{Li}_{1+x}\text{Al}_x\text{Sn}_y\text{Ge}_{2-(x+y)}(\text{PO}_4)_3$. For the sample $\text{LiGe}_2(\text{PO}_4)_3$ the data represent the total conductivity, because only one semicircle is observed in the Nyquist plot.

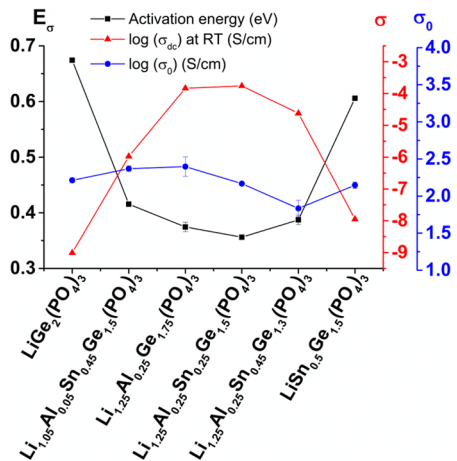


Figure 11. Activation energy (E_σ), room temperature grain conductivity (σ_{dc}) and logarithm of pre-exponential factor ($\log \sigma_0$) of the Arrhenius expression, of the crystalline samples with composition $\text{Li}_{1+x}\text{Al}_x\text{Sn}_y\text{Ge}_{2-(x+y)}(\text{PO}_4)_3$. For the sample $\text{LiGe}_2(\text{PO}_4)_3$ the data represent the total conductivity.

Table 7. Room Temperature dc Electrical Conductivities σ_{dc} , Activation Energies E_σ , and Arrhenius Pre-exponential Factors σ_0 of Crystalline Samples with Compositions $\text{Li}_{1+x}\text{Al}_x\text{Sn}_y\text{Ge}_{2-(x+y)}(\text{PO}_4)_3$

compositions $y = \text{Sn};$ $x = \text{Al}$	$\log[\sigma_{dc}/\text{cm}^{-1}]$		E_σ/eV	$\log \sigma_0/(\text{S}/\text{cm}^{-1})$
	grain	total	grain	grain
$x = 0 y = 0$	-9.01	0.674 ± 0.003^a	2.21 ± 0.03^a	
$x = 0 y = 0.5$	-7.95	-8.61	0.606 ± 0.003	2.15 ± 0.04
$x = 0.05 y = 0.45$	-5.98	-6.03	0.416 ± 0.003	2.37 ± 0.04
$x = 0.25 y = 0.45$	-4.62	-5.49	0.387 ± 0.008	1.80 ± 0.1
$x = 0.25 y = 0.25$	-3.76	-4.41	0.356 ± 0.001	2.17 ± 0.02
$x = 0.25 y = 0$	-3.83	-4.38	0.374 ± 0.008	2.40 ± 0.1

^aIncludes grain and grain boundary contributions.

germanium indeed enhance the grain ionic conductivity. The sample $\text{Li}_{1.25}\text{Al}_{0.25}\text{Sn}_{0.25}\text{Ge}_{1.5}(\text{PO}_4)_3$ exhibits the highest grain electrical conductivity, (1.73×10^{-4} S/cm at room temperature) and the lowest activation energy (0.356 eV) of the present set of solid solutions. On the other hand, for the higher Sn substitution level of $y = 0.45$ we observe an increase in E_σ of grain conductivity, as seen in the literature for high tin substitution levels ($x = 1$) as well.²⁵

Ionic Mobilities. To examine whether the electrical conductivity changes discussed above are related to an enhanced mobility of the Li^+ ions, we studied the static ${}^7\text{Li}$ NMR spectra as a function of temperature, following the approach of previous workers on related lithium containing NASICON phases.^{31–36} In general, one can characterize the ionic mobility of the Li^+ ions by a correlation time τ_c which can be identified as the mean residence time of an ion in a given site. At sufficiently low temperatures τ_c is too long to influence the static ${}^7\text{Li}$ NMR spectrum on the NMR time scale, which is represented by the inverse of the line width $\Delta\omega$ in angular frequency units. In this rigid lattice limit, characterized by $\Delta\omega\tau_c > 1$ a constant line shape is observed, reflecting the anisotropic broadening of the static ${}^7\text{Li}$ resonance by magnetic dipole-dipole interactions and magnetic shielding effects. With increasing temperature, the correlation time decreases

successively, until in the limit $\Delta\omega\tau_c \approx 1$ the ionic motion begins to modulate these interactions, resulting in a continuous narrowing of the ${}^7\text{Li}$ resonance (motional narrowing regime). Finally, in the limit $\Delta\omega\tau_c < 1$, the fast motion regime, the ${}^7\text{Li}$ NMR line width reaches a plateau value, reflecting the residual anisotropic interactions the ${}^7\text{Li}$ spins are still exposed to under the influence of the fast motional averaging process. The onset temperature T_o marking the transition from the rigid lattice limit to the motional averaging regime can be related to the activation energy of the motional process, using the Waugh-Fedin expression: $E_A(\text{meV}) = 1.62T_o$.⁵⁵ Figure 12 summarizes the results obtained on the crystallized samples of the present study. First of all, in the rigid lattice limit, all the Al containing samples show significantly higher fwhm values than the $x = 0$ samples. This effect is expected because of the increased Li concentrations in them, resulting in stronger homonuclear ${}^7\text{Li}-{}^7\text{Li}$ dipole-dipole interaction strengths; also these samples have an extra contribution from ${}^7\text{Li}-{}^{27}\text{Al}$ heteronuclear magnetic dipole interactions to the fwhm. Second, regarding the motional narrowing effects, the onset temperatures observed in the three Al-containing samples are significantly lower than in the two Al-free samples, in agreement with the electrical conductivity data. For these three samples, subtle variations in the temperature dependent line width evolution as a function of temperature suggest that the ionic mobility decreases in the order $\text{Li}_{1.25}\text{Al}_{0.25}\text{Sn}_{0.25}\text{Ge}_{1.5}(\text{PO}_4)_3 > \text{Li}_{1.25}\text{Al}_{0.25}\text{Ge}_{1.75}(\text{PO}_4)_3 > \text{Li}_{1.25}\text{Al}_{0.25}\text{Sn}_{0.45}\text{Ge}_{1.3}(\text{PO}_4)_3$, even though the onset values T_o cannot be determined with sufficient precision to resolve this difference outside of experimental error. We estimate $E_A = 0.27 \pm 0.02$ eV for these three samples. In contrast, for $\text{LiGe}(\text{PO}_4)_3$ and its tin-substituted analogue $\text{LiGe}_{1.5}\text{Sn}_{0.5}(\text{PO}_4)_3$ the estimated activation energies (0.50 ± 0.01 eV and 0.45 ± 0.01 eV) are substantially higher. As a consequence of a distribution of activation energies, omnipresent in disordered electrolytes, the average E_A values estimated from ${}^7\text{Li}$ NMR tend to be somewhat lower compared to the values E_σ obtained from the electrical conductivity measurements.⁵⁶ Nevertheless, the sample trends observed in both sets of measurements closely agree with each other. This result indicates that the electrical conductivity differences of Table 6 indeed reflect differences in ionic mobilities. In particular, the noticeable difference between LGP and $\text{LiGe}_{1.5}\text{Sn}_{0.5}(\text{PO}_4)_3$ supports the idea that ionic mobility and electrical conductivity can be increased by widening the structural bottleneck for lithium ion transfer between sites. The effect can also be realized in Al-containing samples with low Sn contents ($y = 0.25$), even though it is much smaller. It reverses at higher substitution levels ($y = 0.45$), possibly as a consequence of lattice distortions as suggested in the literature.²⁵

The electrical conductivities of the glassy samples are several orders of magnitude lower, with activation energies near 0.8 eV, consistent with previous results on related materials.¹⁵ Likewise, the motional narrowing effect observed in the static ${}^7\text{Li}$ NMR spectra is only observed at significantly higher temperatures, again indicating that the lithium ionic mobilities are considerably lower than in the crystallized samples (see Figure S8, Supporting Information.)

CONCLUSIONS

In summary, the results of the present study show that crystalline solid solutions in the system $\text{Li}_{1+x}\text{Al}_x\text{Sn}_y\text{Ge}_{2-(x+y)}(\text{PO}_4)_3$ may be formed by crystallization of

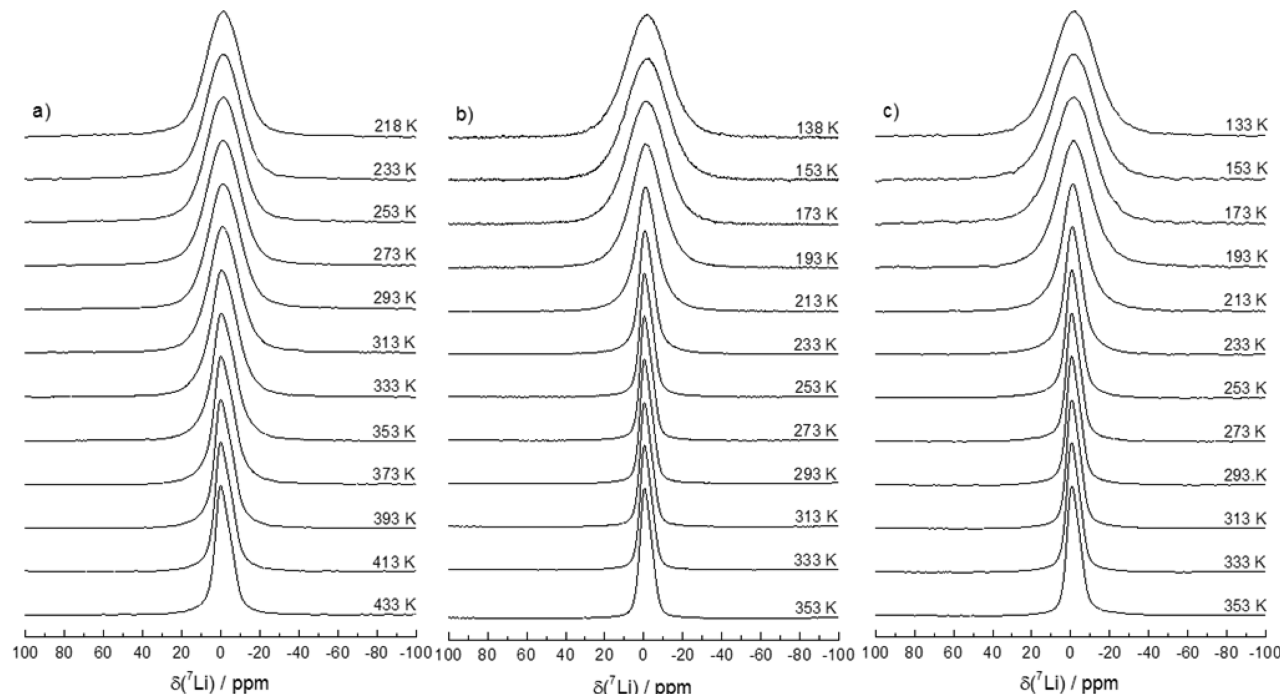


Figure 12. Temperature dependence of ${}^7\text{Li}$ static NMR spectra of (a) $\text{LiGe}(\text{PO}_4)_3$, (b) $\text{Li}_{1.25}\text{Al}_{0.25}\text{Sn}_{0.25}\text{Ge}_{1.5}(\text{PO}_4)_3$, and (c) $\text{Li}_{1.25}\text{Al}_{0.25}\text{Sn}_{0.45}\text{Ge}_{1.3}(\text{PO}_4)_3$, measured at 5.7 T.

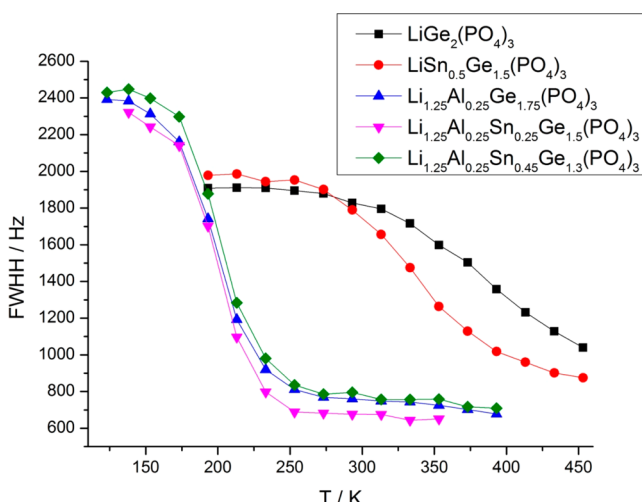


Figure 13. Temperature-dependent full width at half-maximum at 5.7 T of the static ${}^7\text{Li}$ NMR spectra of samples with compositions $\text{Li}_{1+x}\text{Al}_x\text{Sn}_y\text{Ge}_{2-(x+y)}(\text{PO}_4)_3$.

glassy precursor samples. For modest substitution levels ($y = 0.25$), the lattice expansion associated with the substitution of Ge by its larger homologue Sn does produce a (moderate) enhancement of electrical conductivities and ionic mobilities. The structure of the glasses and their crystalline counterparts has been characterized in detail by multinuclear single and double resonance NMR experiments. While substantial changes in the ${}^{31}\text{P}$ and ${}^{27}\text{Al}$ MAS NMR spectra indicate that the crystallization of the glasses is accompanied by significant modifications in the local environments of the phosphate and the aluminum species, the dipolar solid state NMR experiments indicate that the structures of both phases are dominated by Ge–O–P, Sn–O–P, and Al–O–P connectivities. The glass structure is dominated by $\text{P}^{(3)}$ units linked to both four- and six-

coordinated Ge, Al, Sn, as well as P units, whereas the crystal structure contains exclusively $\text{P}^{(4)}$ units linked to six-coordinated Ge, Al, and/or Sn atoms. In the crystalline materials, the ${}^{31}\text{P}$ NMR spectra reveal multiple $\text{P}^{(4)}_{(4-n-m)\text{Ge},(n+m)\text{Al/Sn}}$ sites, with no chemical shift distinction between n and m . Nevertheless, for each resolved resonance characterized by a given value of $(n+m)$ one can extract an average number of P–O–Al linkages using ${}^{31}\text{P}\{{}^{27}\text{Al}\}$ REAP-DOR experiments. Overall, the results of the present study define a useful structural investigation protocol for these compositionally complex superionic conductors.

■ ASSOCIATED CONTENT

S Supporting Information

The Supporting Information is available free of charge on the ACS Publications website at DOI: 10.1021/acs.jpcc.6b04839.

Raman spectra, ${}^{27}\text{Al}$ TQMAS data, ${}^{27}\text{Al}\{{}^{31}\text{P}\}$ REDOR data, ${}^{31}\text{P}$ double quantum NMR spectra, complete impedance plot analyses, and variable temperature ${}^7\text{Li}$ NMR static spectra (PDF)

■ AUTHOR INFORMATION

Corresponding Author

*E-mail: santagneli@iq.unesp.br.

Notes

The authors declare no competing financial interest.

■ ACKNOWLEDGMENTS

We acknowledge funding by FAPESP, Grant 2013/02456-1, and Grant 2013-07793-6 (CEPID program). C.D. and H.E. also acknowledge funding by the Deutsche Forschungsgemeinschaft. S.K. acknowledges the CAPES Young Talent program, through process number 88881.068006/2014-01.

■ REFERENCES

- (1) Scrosati, B.; Hassoun, J.; Sun, Y.-K. Lithium-ion Batteries. A Look into the Future. *Energy Environ. Sci.* **2011**, *4*, 3287–3295.
- (2) Masquelier, C. Solid Electrolytes: Lithium Ions on the Fast Track. *Nat. Mater.* **2011**, *10*, 649.
- (3) Etacheri, V.; Marom, R.; Elazari, R.; Salitra, G.; Aurbach, D. Challenges in the Development of Advanced Li-ion Batteries: a Review. *Energy Environ. Sci.* **2011**, *4*, 3243–3262.
- (4) Knauth, P. Inorganic Solid Li Ion Conductors: An Overview. *Solid State Ionics* **2009**, *180*, 911–916.
- (5) Minami, T.; Hayashi, A.; Tatsumisago, M. Recent Progress of Glass and Glass-Ceramics as Solid Electrolytes for Lithium Secondary Batteries. *Solid State Ionics* **2006**, *177*, 2715–2720.
- (6) Fergus, J. W. Ceramic and Polymeric Solid Electrolytes for Lithium-Ion Batteries. *J. Power Sources* **2010**, *195*, 4554–4569.
- (7) Cao, C.; Li, Z.; Wang, X. L.; Zhao, X.; Han, W. Q. Recent Advances in Inorganic Solid Electrolytes for Lithium Batteries. *Front. Energy Res.* **2014**, *2*, 1–10.
- (8) Fu, J. Fast Ion Conducting Glass Ceramics in the System $\text{Li}_2\text{O}-\text{Al}_2\text{O}_3-\text{GeO}_2-\text{P}_2\text{O}_5$. *Solid State Ionics* **1997**, *104*, 191–194.
- (9) Takada, K. Lithium Ion Conduction in $\text{LiTi}_2(\text{PO}_4)_3$. *Solid State Ionics* **2001**, *139*, 241–247.
- (10) He, K.; Wang, Y.; Zu, C.; Zhao, H.; Liu, Y.; Chen, J.; Han, B.; Ma, J. Influence of Al_2O_3 Additions on Crystallization Mechanism and Conductivity of $\text{Li}_2\text{O}-\text{GeO}_2-\text{P}_2\text{O}_5$ Glass Ceramics. *Phys. B* **2011**, *406*, 3947–3950.
- (11) Feng, J. K.; Yan, B. G.; Liu, J. C.; Lai, M. O.; Li, L. All Solid State Lithium Ion Rechargeable Batteries Using NASICON Structured Electrolyte. *Mater. Technol.* **2013**, *28*, 276–279.
- (12) Yamamoto, H.; Tabuchi, M.; Takeuchi, T.; Kageyama, H.; Nakamura, O. Ionic Conductivity enhancement in $\text{LiGe}_2(\text{PO}_4)_3$ Solid Electrolyte. *J. Power Sources* **1997**, *68*, 397–401.
- (13) Cruz, A. M.; Ferreira, E. B.; Rodrigues, A. C. M. Controlled Crystallization and Ionic Conductivity of a Nanostructured LiAlGePO_4 Glass-Ceramic. *J. Non-Cryst. Solids* **2009**, *355*, 2295–2301.
- (14) Arbi, K.; Bucheli, W.; Jimenez, R.; Sanz, J. High Lithium Ion Conducting Solid Electrolytes Based on NASICON $\text{Li}_{1+x}\text{Al}_x\text{M}_{2-x}(\text{PO}_4)_3$ Materials ($\text{M} = \text{Ti}, \text{Ge}$, and $0 \leq x \leq 0.5$). *J. Eur. Ceram. Soc.* **2015**, *35*, 1477–1484.
- (15) Narvaez-Semanate, J. L.; Rodrigues, A. C. M. Microstructure and Ionic Conductivity of $\text{Li}_{1+x}\text{Al}_x\text{Ti}_{2-x}(\text{PO}_4)_3$ NASICON Glass-Ceramics. *Solid State Ionics* **2010**, *181*, 1197–1204.
- (16) Arbi, K.; Mandal, S.; Rojo, J. M.; Sanz, J. Dependence of Ionic Conductivity on Composition of Fast Ionic Conductors $\text{Li}_{1+x}\text{Ti}_{2-x}\text{Al}_x(\text{PO}_4)_3$ ($0 < x < 0.7$). A Parallel NMR and Electric Impedance Study. *Chem. Mater.* **2002**, *14*, 1091–1097.
- (17) Shimonishi, Y.; Zhang, T.; Imanishi, N.; Lee, D. J.; Hirano, A.; Takeda, Y.; Yamamoto, O.; Sammes, N. A Study on Lithium/Air Secondary Batteries-Stability of the NASICON-Type Lithium Ion Conducting Solid Electrolyte in Alkaline Aqueous Solutions. *J. Power Sources* **2011**, *196*, 5128–5132.
- (18) Hasegawa, S.; Imanishi, N.; Zhang, T.; Xie, J.; Hirano, A.; Takeda, Y.; Yamamoto, O. Study on Lithium/Air Secondary Batteries-Stability of NASICON-Type Lithium Ion Conducting Glass-Ceramics with Water. *J. Power Sources* **2009**, *189*, 371–377.
- (19) Imanishi, N.; Matsui, M.; Takeda, Y.; Yamamoto, O. Lithium Ion Conducting Solid Electrolytes for Aqueous Lithium-Air Batteries. *Electrochemistry* **2014**, *82*, 938–945.
- (20) Safanama, D.; Damiano, D.; Rao, R. P.; Adams, S. Lithium Conducting Solid Electrolyte $\text{Li}_{1+x}\text{Al}_x\text{Ge}_{2-x}(\text{PO}_4)_3$ Membrane for Aqueous Lithium Air Battery. *Solid State Ionics* **2014**, *262*, 211–215.
- (21) Zhang, P.; Wang, H.; Lee, Y. G.; Matsui, M.; Takeda, Y.; Yamamoto, O.; Imanishi, N. Tape Cast Water Stable NASICON Type High Lithium Ion Conducting Solid Electrolyte Films for Aqueous Lithium-Air Batteries. *J. Electrochem. Soc.* **2015**, *162*, A1265–A1271.
- (22) Xu, X. X.; Wen, Z. Y.; Gu, Z. H.; Xu, X. H.; Lin, Z. X. Lithium Ion Conductive Glass Ceramics in the System $\text{Li}_{1.4}\text{Al}_{0.4}(\text{Ge}_{1-x}\text{Ti}_x)_{1.6}(\text{PO}_4)_3$ ($x = 0–1.0$). *Solid State Ionics* **2004**, *171*, 207–213.
- (23) Xu, X.; Wen, Z. Y.; Gu, Z. H.; Lin, Z. X. High Lithium Conductivity in $\text{Li}_{1.3}\text{Cr}_{0.3}\text{Ge}_{1.7}(\text{PO}_4)_3$ Glass Ceramics. *Mater. Lett.* **2004**, *58*, 3428–3431.
- (24) Zhang, P.; Wang, H.; Si, Q.; Matsui, M.; Takeda, Y.; Yamamoto, O.; Imanishi, N. High Lithium Conductivity Solid Electrolyte of Chromium and Aluminum Doped NASICON -type $\text{LiTi}_2(\text{PO}_4)_3$. *Solid State Ionics* **2015**, *272*, 101–106.
- (25) Francisco, B. E.; Stoldt, C. R.; M'Peko, J. C. Lithium Ion Trapping from Local Structural Distortions in Sodium Super Ionic Conductor (NASICON) Electrolytes. *Chem. Mater.* **2014**, *26*, 4741–4749.
- (26) Xu, X.; Yang, T.; Lu, Z.; Gao, S.; Shu, H. J.; Zheng, W.; Cheng, L.; Feng, L.; Ren, Y. The Preparation and Lithium Mobility of Zinc Based NASICON -Type Solid Electrolyte $\text{Li}_{1+2x+2y}\text{Al}_x\text{Zn}_y\text{Ti}_{2-x}\text{Si}_x\text{P}_{3-x}\text{O}_{12}$. *Ceram. Int.* **2014**, *40*, 3819–3822.
- (27) Wong, S.; Newman, P. J.; Best, A. S.; Nairn, K. M.; Macfarlane, D. R.; Forsyth, M. Towards Elucidating Microscopic Structural Changes in Li Ion Conductors $\text{Li}_{1+y}\text{Ti}_{2-y}\text{Al}_y(\text{PO}_4)_3$ and $\text{Li}_{1+y}\text{Ti}_{2-y}\text{Al}_y(\text{PO}_4)_{3-x}(\text{MO}_4)_x$ ($\text{M} = \text{V}$ and Nb): X-ray and ^{27}Al and ^{31}P NMR Studies. *J. Mater. Chem.* **1998**, *8*, 2199–2203.
- (28) Forsyth, M.; Wong, S.; Nairn, K. M.; Best, A. S.; Newman, P. J.; MacFarlane, D. R. NMR Studies of Modified NASICON-Like Lithium Ion Solid Electrolytes. *Solid State Ionics* **1999**, *124*, 213–219.
- (29) Maldonado-Manso, P.; Martin-Sedeno, M. C.; Bruque, S.; Sanz, J.; Losilla, E. R. Unexpected Cationic Distribution in Tetrahedral/Octahedral Sites in Nominal $\text{Li}_{1+x}\text{Al}_x\text{Ge}_{2-x}(\text{PO}_4)_3$ NASICON Series. *Solid State Ionics* **2007**, *178*, 43–52.
- (30) Maldonado-Manso, P.; Losilla, E. R.; Martinez-Lara, M.; Aranda, M. A. G.; Bruque, S.; Mouahid, F. E.; Zahir, M. High Lithium Ionic Conductivity in the $\text{Li}_{1+x}\text{Al}_x\text{Ge}_y\text{Ti}_{2-x-y}(\text{PO}_4)_3$ NASICON Series. *Chem. Mater.* **2003**, *15*, 1879–1885.
- (31) Katoh, T.; Inda, Y.; Baba, M.; Ye, R. Lithium Ion Conductive Glass Ceramics with Composition Ratio Control and their Electrochemical Characteristics. *J. Ceram. Soc. Jpn.* **2010**, *118*, 1159–1162.
- (32) Pinus, Y.; Khoroshilov, A. V.; Gavrichov, K. S.; Tarasov, V. P.; Yaroslavtsev, A. B. On cationic mobility in NASICON Phosphates $\text{LiTi}_2(\text{PO}_4)_3$ and $\text{Li}_{0.9}\text{Ti}_{1.9}\text{Nb}_{0.1}(\text{PO}_4)_3$. *Solid State Ionics* **2012**, *212*, 112–116.
- (33) Schröder, C.; Ren, J.; Rodrigues, A. C. M.; Eckert, H. Glass-to-Crystal Transition in $\text{Li}_{1+x}\text{Al}_x\text{Ge}_{2-x}(\text{PO}_4)_3$: Structural Aspects Studied by Solid State NMR. *J. Phys. Chem. C* **2014**, *118*, 9400–9411.
- (34) Liu, Z.; Venkatachalam, S.; van Wüllen, L. Structure, Phase Separation and Li Dynamics in Sol-Gel-Derived $\text{Li}_{1+x}\text{Al}_x\text{Ge}_{2-x}(\text{PO}_4)_3$. *Solid State Ionics* **2015**, *276*, 47–55.
- (35) Barre, M.; Emery, J.; Florian, P.; Le Berre, F.; Crosnier-Lopez, M. P.; Fourquet, J. L. NMR Investigations of Li Ion Dynamics in the NASICON Ionic Conductors $\text{Li}_{1-x}\text{La}_x\text{Zr}_2(\text{PO}_4)_3$. *J. Phys.: Condens. Matter* **2009**, *21*, 175404.
- (36) Paris, M. A.; Sanz, J. Structural Changes in the compounds $\text{LiM}_2(\text{PO}_4)_3$ ($\text{M} = \text{Ge}, \text{Ti}, \text{Sn}$, and Hf) as Followed by ^{31}P and ^{7}Li NMR. *Phys. Rev. B: Condens. Matter Mater. Phys.* **1997**, *55*, 14270–14278.
- (37) Arbi, K.; Paris, M. A.; Sanz, J. Li Mobility in Nasicon Type Materials $\text{LiM}_2(\text{PO}_4)_3$, $\text{M} = \text{Ge}, \text{Ti}, \text{Sn}, \text{Zr}$, and Hf , Followed by ^{7}Li NMR Spectroscopy. *Dalton Trans.* **2011**, *40*, 10195–10202.
- (38) Arbi, K.; Tabellout, M.; Lazarraga, M. G.; Rojo, J. M.; Sanz, J. Non-Arrhenius Conductivity in the Fast Lithium Conductor $\text{Li}_{1.2}\text{Ti}_{1.8}\text{Al}_{0.2}(\text{PO}_4)_3$: A ^{7}Li NMR and Electric Impedance Study. *Phys. Rev. B: Condens. Matter Mater. Phys.* **2005**, *72*, 094302.
- (39) Lang, B.; Ziebarth, B.; Elsässer, C. Lithium Ion Conduction in $\text{LiTi}_2(\text{PO}_4)_3$ and Related Compounds Based on the NASICON Structure: A First Principles Study. *Chem. Mater.* **2015**, *27*, 5040–5048.
- (40) Massiot, D.; Fayon, F.; Capron, M.; King, I.; Le Calvé, S.; Alonso, B.; Durand, J. O.; Bujoli, B.; Gan, Z.; Hoatson, G. Modelling One- and Two-dimensional solid-state NMR spectra. *Magn. Reson. Chem.* **2002**, *40*, 70–76.
- (41) Medek, A.; Harwood, J. S.; Frydman, L. Multiple-Quantum Magic-Angle Spinning NMR: A New Method for the Study of

- Quadrupolar Nuclei in Solids. *J. Am. Chem. Soc.* **1995**, *117*, 12779–12787.
- (42) Amoureaux, J. P.; Fernandez, C.; Steuernagel, S. Z Filtering in MQMAS NMR. *J. Magn. Reson., Ser. A* **1996**, *A123*, 116–118.
- (43) Gullion, T.; Schaefer, J. Rotational Echo Double Resonance NMR. *J. Magn. Reson.* **1989**, *81*, 196–200.
- (44) Chopin, L.; Vega, S.; Gullion, T. A MAS NMR Method for Measuring ^{13}C - ^{17}O Distances. *J. Am. Chem. Soc.* **1998**, *120*, 4406–4409.
- (45) Gullion, T.; Vega, A. Measuring Heteronuclear Dipolar Couplings for $I = 1/2$, $S > 1/2$ Spin Pairs by REDOR and REAPDOR NMR. *Prog. Nucl. Magn. Reson. Spectrosc.* **2005**, *47*, 123–126.
- (46) Bertmer, M.; Eckert, H. Dephasing of Spin Echoes by Multiple Dipolar Interactions in Rotational Echo Double Resonance NMR Experiments. *Solid State Nucl. Magn. Reson.* **1999**, *15*, 139–152.
- (47) Bak, M.; Rasmussen, J. T.; Nielsen, N. C. SIMPSON: A General Simulation Program for Solid-State NMR Spectroscopy. *J. Magn. Reson.* **2000**, *147*, 296–330.
- (48) Ganschow, M.; Schulz-Ekloff, G.; Wark, M.; Wendschuh-Josties, M.; Wöhrle, D. Microwave-Assisted Preparation of Uniform Pure and Dye-Loaded $\text{AlPO}_4 - 5$ Crystals with Different Morphologies for Use as Microlaser Systems. *J. Mater. Chem.* **2001**, *11*, 1823–1827.
- (49) Phani, A. R.; Di Claudio, D.; Passacantando, M.; Santucci, S. GeO_2 Based High k Dielectric Material Synthesized by Sol – Gel Process. *J. Non-Cryst. Solids* **2007**, *353*, 692–696.
- (50) Winand, J. M.; Rulmont, A.; Tarte, P. Nouvelles Solutions Solides $\text{LI}(\text{MIV})_{2-x}(\text{NIV})_x(\text{PO}_4)_3$ ($\text{L} = \text{Li}, \text{Na}$ M,N = Ge,Sn,Ti,Zr,Hf). Synthèse et Etude par Diffraction x et Conductivité Ionique. *J. Solid State Chem.* **1991**, *93*, 341–349.
- (51) Behrends, F.; Eckert, H. Mixed Network Former Effects in Oxide Glasses: Structural Studies in the System $(\text{M}_2\text{O})_{1/3}[(\text{Ge}_2\text{O}_4)_x(\text{P}_2\text{O}_5)_{1-x}]_{2/3}$ by Solid State NMR Spectroscopy. *J. Phys. Chem. C* **2014**, *118*, 10271–10283.
- (52) Francisco, B. E.; Stoldt, C. R.; M'Peko, J. C. Energetics of Ion Transport in NASICON-Type Electrolytes. *J. Phys. Chem. C* **2015**, *119*, 16432–16442.
- (53) Idris, S.; Scheuermann, M.; Becker, S. M.; Sepelak, V.; Kruk, R.; Suffner, J. Local Structural Disorder and Relaxation in SnO_2 Nanostructures Studied by ^{119}Sn MAS NMR and ^{119}Sn Mössbauer Spectroscopy. *J. Phys. Chem. C* **2011**, *115*, 6433–6437.
- (54) Bekaert, É.; Montagne, L.; Delevoye, L.; Palavit, G.; Revel, B. Structure and Properties of $x \text{ SnO} - (100 - x) \text{ P}_2\text{O}_5$ Glasses. *C. R. Chim.* **2004**, *7*, 377–382.
- (55) Waugh, J. S.; Fedin, I. E. Determination of Hindered Rotation Barriers in Solids. *Solid State Commun.* **1963**, *4*, 1633–1636.
- (56) Storek, M.; Böhmer, R.; Martin, S. W.; Larink, D.; Eckert, H. NMR and Conductivity Studies of the Mixed Glass-Former Effect in Lithium Borophosphate Glasses. *J. Chem. Phys.* **2012**, *137*, 124507.